International Journal of Fatigue 178 (2024) 108018

Contents lists available at ScienceDirect

International Journal of Fatigue

journal homepage: www.elsevier.com/locate/ijfatigue

Fatigue strength estimation of net-shape L-PBF Co–Cr–Mo alloy via non-destructive surface measurements

S. Romano [a,*], E. Peradotto [a], S. Beretta [b], D. Ugues [c], L. Barricelli [b], G. Maculotti [d], L. Patriarca [b], G. Genta [d]

[a] GE Avio s.r.l., Via Primo Maggio 99, 10040, Rivalta di Torino (TO), Italy
[b] Department of Mechanical Engineering, Politecnico di Milano, via La Masa 1, 20156, Milano (MI), Italy
[c] Department of Applied Science and Technology, Politecnico di Torino, Corso Duca degli Abruzzi 24, 10129, Torino (TO), Italy
[d] Department of Management and Production Engineering, Politecnico di Torino, Corso Duca degli Abruzzi 24, 10129, Torino (TO), Italy

ARTICLE INFO

Keywords:
L-PBF
Co–Cr–Mo
Surface quality
Fatigue
NDT
4-points bending

ABSTRACT

One of the primary challenges in utilizing additive manufacturing for load-bearing metal components in the aerospace industry lies in the relatively low fatigue strength and significant variability stemming from the typically rough as-built surfaces. The goal of this research is to develop a model able to robustly correlate parameters obtained by non-destructive measurements to the fatigue strength of a generic surface state for a cobalt-chrome alloy manufactured via laser powder bed fusion (L-PBF). The results show that a relatively accurate estimation of fatigue strength of a generic surface quality can be performed via high-quality non-destructive roughness measurements coupled with statistical considerations and fracture mechanics-based assessments. This provides the capability of comparing different surface states and selecting the best option for fatigue strength with limited experimental effort and might prospectively set the basis for qualification of L-PBF components in the presence of rough surfaces.

1. Introduction

Fatigue properties of additively manufactured (AM) materials are mainly driven by anomalies [1,2]. Although the comprehension of defect formation [3] and the development of optimized machine parameters for hatch filling and contouring allows minimizing frequency and size of porosity and lack of fusion, obtaining completely anomaly-free structures remains challenging with current technologies. Internal porosity can generally be closed via hot isostatic pressing (HIP). After HIP, the vast majority or the totality of fatigue failures are driven by the surface state. As 100% machining on AM parts would hinder exploiting some of the main advantages of the technology (i.e., shape complexity, ability to manufacture thin walls and internal channels), significant effects caused by as-printed surface state shall be accounted by design.

Considering laser powder bed fusion (L-PBF), surface roughness in the as-printed condition is generally much larger compared to conventional manufacturing. Surface features (stair-case effect [4], cavities, asperities, waviness [5]) act as local stress raiser introducing debits on fatigue strength as large as 40%–60% of conventionally machined condition [6]. Due to the stress concentration effects of the deepest/most critical surface features, it is then clear that average line roughness parameters are not well correlated to the fatigue strength of AM materials [7,8]. Recent literature has shown that the most significant roughness parameter (in terms of correlation with fatigue lives or fatigue strength) is the maximum profile valley depth parameter R_v or S_v [9] for linear or areal measurements respectively, or some modification of it [10]. Such correlations are usually helpful in a qualitative way only and it is doubtful, as it happens for AI-based analyses [11], if it is possible to extrapolate the predictions to textures/anomaly sizes different from the ones in the testing databases. However, no clear evidence of the correlation between roughness-based measurements and the size of the anomaly at the origin of fatigue failure is provided. Similarly, approaches based on equivalent initial flaw size (EIFS) [12] can provide the interpretation of tests and the influence of feature size or surface residual stresses [13], but they are not based on measured surface features.

On the other hand, fracture-based analyses have been extensively and successfully applied to net-shape surfaces adopting profile valley depth as the relevant parameter for initial flaw size and modelling the surface features as 'short cracks' [14–19], even based on X-ray micro computed tomography (μ-XCT) measurements of the surface features at the origin of fatigue failure [20,21]. As compared to other analyses based on *fatigue notch factor* [22–24], the fracture-based

* Corresponding author.
E-mail address: simone.romano@avioaero.it (S. Romano).

https://doi.org/10.1016/j.ijfatigue.2023.108018
Received 9 July 2023; Received in revised form 16 September 2023; Accepted 20 October 2023
Available online 26 October 2023

Table 1
Comparison of roughness measurement techniques in AM.

Measurement method	Type of information	Features of main technologies
Contact stylus (CS) [35]	Profile topography measurement	Unless the topography is simple, and characterized by a dominant lay, profile-based measurements are intrinsically limited in their representativeness capability. Furthermore, the mechanical surface is inherently filtered by the convolution introduced by the tip, resulting in systematic errors in the measurement of sharp and steep topographical features.
Confocal Microscopy (CM) [29,36] Focus Variation microscopy (FV) [37] Coherence Scanning Interferometry (CSI) [28,38–40] Conoscopic holography [41] Atomic Force Microscopy (AFM) [42] Elastomeric sensor [43]	Areal topography measurement	The larger and more densely sampled area allows for a more statistically representative and robust measurement. Technologies interact differently with specific AM surface features. CM and FV technologies can be challenged by the highly irregular nature of the typical topographies being measured, but the acquisition time is significantly less than raster-scanned techniques (e.g., AFM). CM and FV can manage high roughness, but may introduce some systematic errors in measurements of peaks and valleys of AM surfaces CSI: highly irregular AM surfaces can present challenges in terms of local slope and vertical scale of roughness [44]. These may be compensated by ad-hoc measurement techniques [38] enabling high accuracy counterbalanced by extremely long measurement time
(micro)X-ray computed tomography (μ-XCT) [33,45–47]	Volumetric measurement	Surface information can be extracted from volumetric data with no limitations due to vertical walls and undercuts. The main hurdles to the widespread adoption of μ-XCT as a mean of measuring surfaces of AM parts reside in currently poor spatial resolutions of the measurement, and lack of complete understanding of metrological performance and error sources, which are necessary for a proper calibration of the surface extraction algorithms (mainly based on thresholding/edge detection) [32,34,48]

methods have the advantage of being adopted for component assessment/qualification [2,25,26]. Therefore, they seem to be more directly applicable to the assessment of the *fatigue quality* of net-shape AM parts by surface roughness measurements and to the acceptability of unintentionally processed (defined as *process escape* condition in [27]) surfaces.

Besides surface topography, subsurface or surface-connected anomalies can behave as preferential points for crack initiation [5,28]. Consequently, their detection can be difficult via conventional contact-based measurement methods [29,30]. Several measurement methods can be adopted to overcome the limitations of profilometry, e.g., non-contact surface characterization via Confocal microscopy (CM), Focus variation microscopy (FV), Coherence scanning interferometry (CSI), or volumetric inspections via X-ray micro computed tomography (μ-XCT) [31–33]. Recent literature has shown that the several available technologies present different capabilities in measuring the surface of AM components, thus introducing statistically significant differences among the results [32,34]. Table 1 briefly summarizes the main limitation of the most widely applied measurement techniques in AM.

Actually, there are no literature data that show clearly a comparison between roughness measurements and size of surface features at the origin of the failures in net-shape surfaces and, consequently, how precise the estimated fatigue strength could be for a given AM surface.

The goal of this research is to cover this gap and to develop a model able to robustly correlate parameters obtained by non-destructive measurements to the fatigue strength of a generic surface state for a cobalt–chrome–molybdenum alloy manufactured via L-PBF in different orientations. This is achieved by characterizing the surface quality of a variety of surface conditions through destructive and non-destructive techniques. Experimental observations are finally correlated to the results of fatigue testing on 4-point bending specimens through a fracture-based fatigue model, where surface topography is accounted for in terms valley depth.

2. Experiments and methods

Multiple series of 4PB specimens in Co–Cr–Mo alloy were manufactured along different orientations respect to the base plate, in order to mimic the various features of a real component, as shown in Fig. 2.

Details about specimen manufacturing are reported in Section 2.1. The test articles were investigated by means of non-destructive measurements (μ-XCT and different roughness measurements reported in Sections 2.2 and 2.3) before and after the fatigue tests, then analysed to reveal the features at the origin of failures (Section 2.4.1). Fig. 1 provides an overview of the experiments and methods.

2.1. Print and specimen manufacturing

Tested specimens were manufactured in the GE Avio's laboratory TAL (Turin Additive Lab.) dedicated to additive components industrialization, qualified according to aerospace specifications and approved for the production of flight-worthy hardware. The machine used was a GE Additive Concept Laser M2 Series 5, with a build volume of 245 × 245 × 350 mm (x, y, z) and 2 lasers of power 1 kW each. The machine was utilized on a single laser mode on each sample (no laser stitching utilized). GE machine operators ensured a correct calibration, maintenance and environmental conditions during the manufacturing of the specimens.

Powder material utilized was Co–Cr–Mo Cobalt-28 Chromium-6 Molybdenum alloy [49] developed and characterized by GE Aerospace for the production of certified components, such as the CFM Leap fuel nozzle tip. Powder source, size, composition, and reuse conformed to production standards. More details can be found at [50].

Melting process parameters, such as laser power, spot size, travel speed and laser dwell time, in combination to hatch strategy for internal areas and external surfaces were set as per production standard. Particular attention has been kept during the slicing process to reproduce on the testing surface of each sample a thermal history and phases transition close to a real production part.

The full set of specimens was printed on four different jobs, mixing inclinations and types to avoid statistical clustering on a specific job or plate position. Horizontal specimens were supported with vertical lamellar support, then removed manually. Vertical (V), upskin (U), and downskin (D) specimens were printed with a "wing" support, not attached to the specimens. The intent of such support is engaging the rake prior to the testing surface and increasing the thermal stability of the print. An example of such disposition is given in Fig. 3.a, while a detail of the wing support is provided in Fig. 3.b.

Fig. 3.c provides the drawing of the 4PB coupon, while Table 2 summarizes the differences between the series of specimens investigated.

Post-processing operations included powder evacuation, vacuum stress relief, platform removal by electro-discharge machining, HIP, and solubilization heat treatment. The specimens were then subjected to accurate machining for ensuring tight planarity tolerances between the contact surfaces for load and support rollers. 0.5 mm × 45° chamfers were eventually ground on all sides of the specimens' tested surface to avoid failures from corner cracks.

Table 2 provides a summary of the 7 series of 4PB fatigue specimens manufactured. Each series is composed of 12 coupons. The inclination angle is evaluated clockwise with respect to the build plate (horizontal

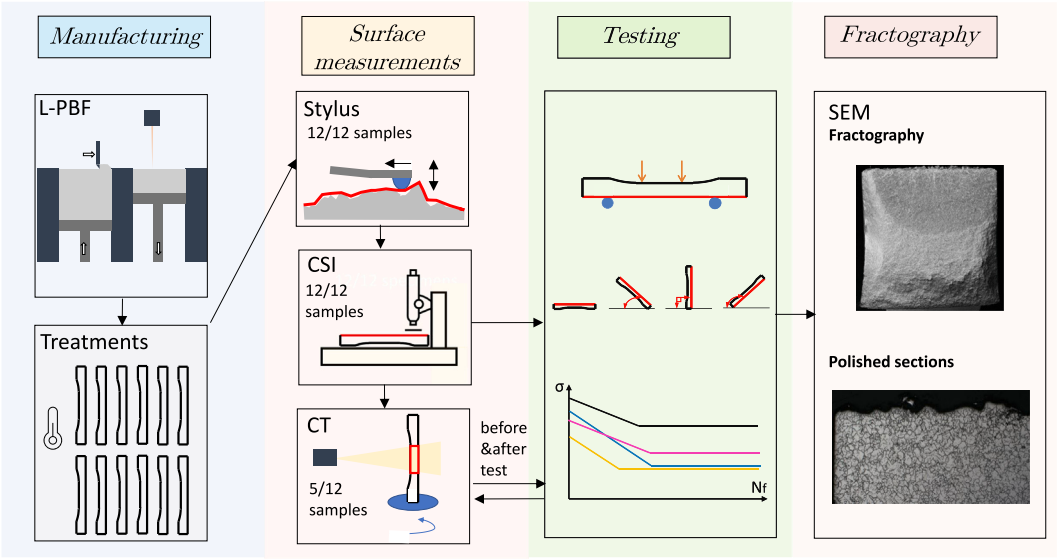

Fig. 1. Manufacturing, testing and post-testing steps for a series.

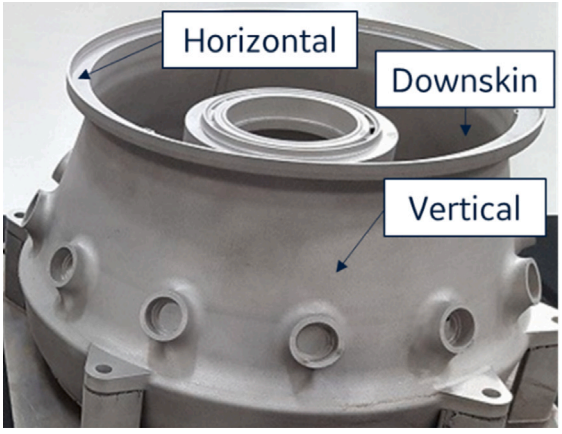

(a)

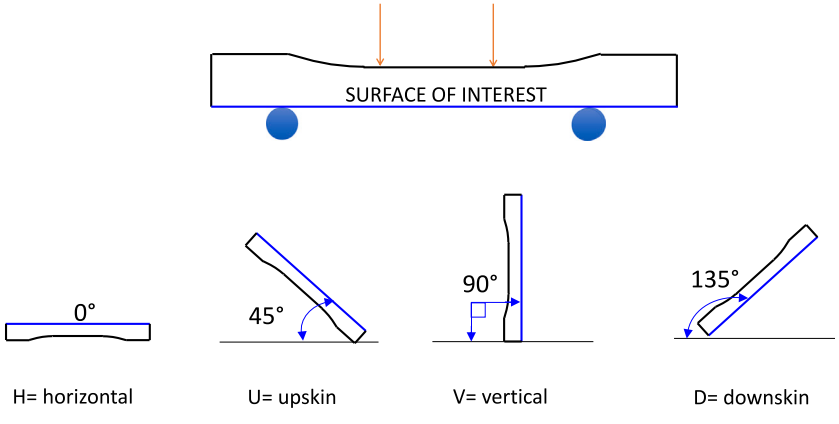

(b)

Fig. 2. Scheme of build orientations related to L-PBF technology: (a) example surface orientation of a component [51]; (b) orientation of specimens manufactured within this research activity. The blue line represents the surface of interest for fatigue strength assessment, which is subjected to maximum stress in this four-points bending configuration. The inclination angle of the surface of interest with respect to the build-plate is indicated.

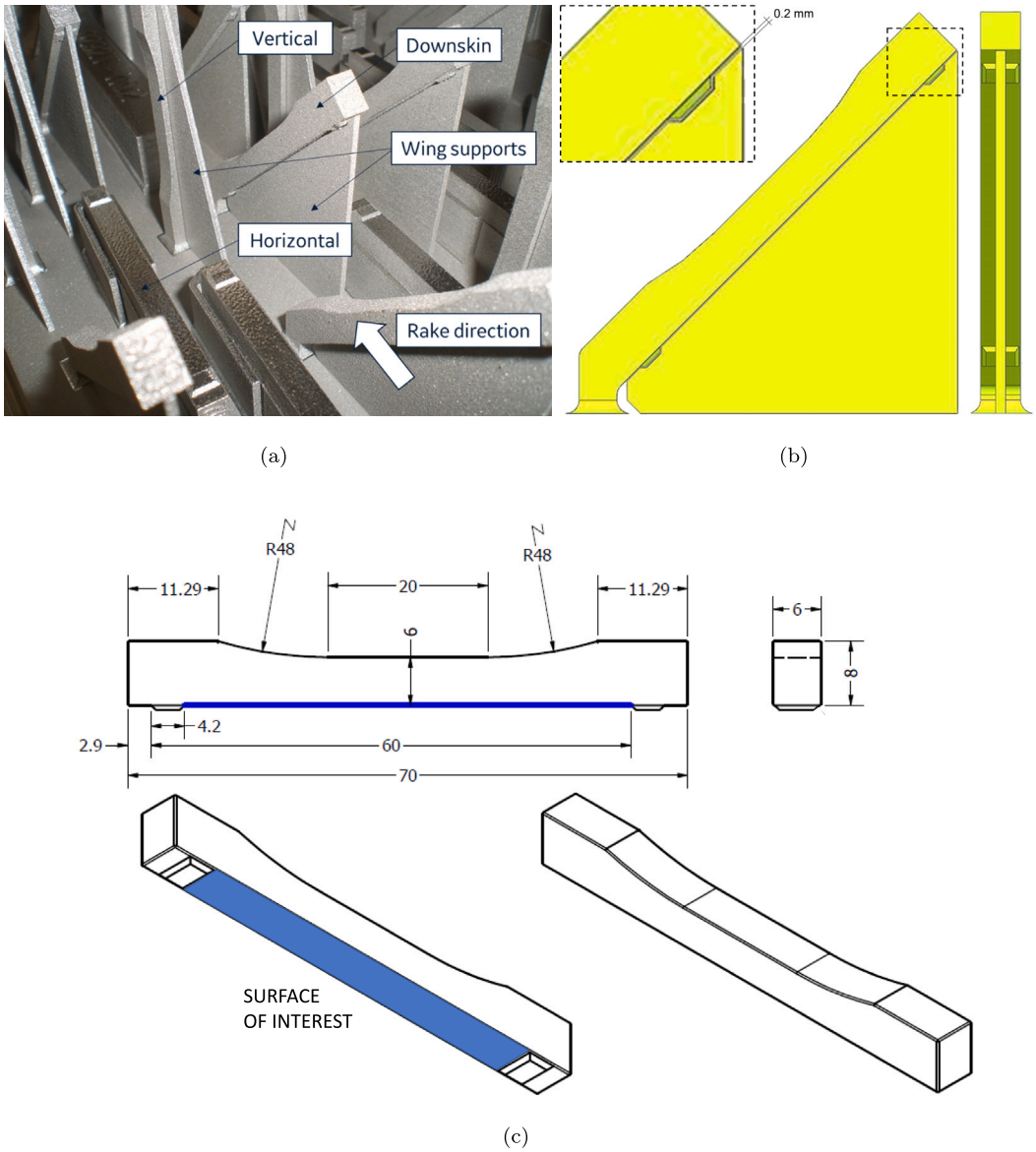

Fig. 3. Detail of 4PB specimens: (a) L-PBF built disposition and configuration; (b) Detail of wing support on downskin specimen; (c) Technical drawing highlighting the surface subjected to maximum stress (dimensions are in mm).

Table 2
Detail of the specimens orientation and condition for each series.

Series	Surface status	Orientation	Angle	Contouring
M	Machined	Vertical	90°	Yes
H	As-built	Horizontal	0°	Yes
V	As-built	Vertical	90°	Yes
U	As-built	Upskin	45°	Yes
D	As-built	Downskin	135°	Yes
H_{nc}	As-built	Horizontal	0°	No
D_{nc}	As-built	Downskin	135°	No

plane), as shown in Fig. 2.b. In order to quantify the effect of contouring strategy, two as-built series (horizontal and downskin) were printed without contouring. These are labelled with the subscript "nc".

2.2. X-ray tomography

X-ray micro-computed tomography (μ-XCT) scans were performed at the Stellenbosch CT scanner facility. A high-resolution scan of the gauge length was performed at 12.5 μm voxel size at 200 kV, 50 μA and 0.2 mm Cu filter with a General Electric VTomex L 240 kV (General Electric Sensing and Inspection Technologies Phoenix X-ray, Wunstorff, Germany). Reconstruction was performed using system-supplied DATOS 2.0 software. Image processing, including post-process alignment and evaluation of crack formation after fatigue testing, was performed using VGSTUDIO MAX 3.5 software (Volume Graphics GmbH, Heidelberg, Germany). The scan parameters were optimized for the sample type considering X-ray penetration, image quality obtained and voxel size. Co–Cr–Mo alloy is very strongly absorbing for X-rays, making it challenging to find suitable parameters. A smaller voxel size would lead to many artefacts while a larger voxel size would not give sufficient detail detectability on surface features.

Coupons were investigated before and after fatigue testing as reported in [52]. The μ-XCT analysis was performed on 5 specimens from all 6 series left in as-printed state using the procedure described below. A total of 60 scans was performed on 30 unique specimens. An initial de-noising was applied using Gaussian 3 × 3x3 filter followed by advanced surface determination to precisely define the edge between material and air. This used an initial global threshold automatically selected based on the grey scales in the data, which locally refines the threshold based on the local grey values.

For each "before" sample, a region of interest on the flat surface was then selected for analysis which includes the whole surface region subjected to maximum stress. A best-fit plane was selected across this region, and a CAD geometry defined from the plane. The deviation between the plane and the actual surface was then calculated using a nominal-actual comparison. From this analysis, the statistical deviation provides information that can be used to extract roughness parameters as described in Section 2.3.

To evaluate the effect of surface anomalies, specimens before and after fatigue testing were aligned and compared to identify crack locations in the "after" scan in relation to surface features present in the "before" scan. Crack initiation locations were identified in "after" scans using optimized 2D contrasted images along all three axes and scrolling through the full data. Markers were placed on these locations on the surface, and the aligned "before" state was evaluated in comparison. The results of μ-XCT analyses are described in Section 3.2.

2.3. Topography characterization

Surface topographies were measured by CSI with a state-of-the-art Zygo NewView 9000 hosted at the facilities of the MInd4Lab at Politecnico di Torino. The instrument was equipped with a 5.5× Michelson objective (numerical aperture 0.15) and a digital 0.5× zoom, having a squared pixel of (3.15 × 3.15) μm and field of view (FOV) of (3.15 × 3.15) mm. The central portion of the surface was measured by stitching 8 × 2 FOVs, resulting in a measured area of (23 × 4) mm. No signal oversampling nor averaging was applied, for the measured surface quality was deemed sufficient due to the very low number of non-measured points [38]. The surface characterization was performed according to the ISO 25178-2 [53] on the scale-limited surface (SL-Surface) by applying a robust Gaussian filter with nesting index 10 μm for denoising and small scale elimination, F-operator to remove form by least square plane fitting, and robust Gaussian L-filter to eliminate waviness with nesting index of 2.5 mm. Nesting indexes were selected according to the standard prescriptions given in ISO25178-3 [54]. Prior to the F-operator application, non-measured points and measurement disturbances were removed with the gaussian process regression method [55].

Similarly, topographies measured by μ-XCT were characterized following the same methodology. Fig. 9.a provides an example of roughness analysis performed via μ-XCT. Considering the resolution of the tomographic measurement, the nesting indexes were set to 80 μm and 2.5 mm, respectively for the S-filter and the L-filter [54]. The analysis aims to assess the sensitivity and systematic differences, already known from the literature (see Table 1), of the two areal surface topography measuring methods with respect to the building direction, whose effect is currently unreported in the literature.

Furthermore, profile measurements were performed to estimate the sensitivity and representativeness of the surface topography measurement method in assessing the severity of the anomalies at the origin of failure. In particular, 5 contact stylus (CS) measurements were performed parallel to the longitudinal side of the specimen surface. As common practice in literature, despite the liability of severe scatter in the results and under-sampling the optical surface, 60 profiles were extracted from the CSI-measured surfaces. Profiles (both resulting from the CS measurement and the sampling of the optical surface) were analysed according to the ISO4288 standard [56] with a sampling length of 0.8 mm for H surfaces and of 2.5 mm for others, and an evaluation length of five times larger than the sampling length. The roughness profile is characterized after the application of a Gaussian filter with a cut-off equal to the sampling length.

Measured surfaces and profiles are characterized in terms of arithmetic mean height (Sa, Ra), root mean square height (Sq, Rq), Skewness (Ssk, Rsk), Kurtosis (Sku, Rku), maximum height (Sz, Rz), maximum valley/pit depth (Sv, Rv), and root mean square gradient Sdq. Evaluation of parameters is performed by state of the art commercial software MountainsLab v8.1. Additionally, the mean parameters Rpm and RSm parameters will be evaluated on profiles (either measured by contact stylus or extracted from topographical measurements), respectively representing the average of the maximum peak height and the average of the spacing of profile features. A non-standard method for the calculation of the spacing parameter RSm is adopted in accordance with the works of Scott and Seewig [57,58]. The issues with the standard definition of RSm arise during the implementation because the definition can be ambiguously interpreted when additive manufactured surfaces are considered. Seewig and Scott proposed unambiguous algorithms for calculating RSm, which allowed distinguishing the relevant profile elements for the spacing and deleting the insignificant ones based on clear criteria and on quantitative thresholds for the discrimination.

Literature links anomalies at the origin of failure with topographical valleys [21,59,60]. Therefore, the comparison of instrument representativeness and measurement robustness will be performed on the basis of the maximum valley/pit depth, i.e., Sv for the surfaces and Rv for the profiles. Other parameters will be reported in Appendix to support the discussion.

An essential feature to enable a fair comparison is to ensure that the same length scale is considered. Therefore, a scale-limited surface resulting from the application of both denoising (S-filter) and large scale filtering (L-filter), shall be considered to tie the evaluation of the critical valley to the roughness profile [6,10,52,61]. However, it is apparent that filtering removes a certain surface variability, and stronger filtering results in reduced height ranges (Sz) which is the upper limit for the maximum valley depth Sv. Thus, the effect of filtering on the estimation of the surface parameter to the approximation of the fractography damage estimation is also considered. Specifically, Sv is evaluated on the SL-surface and on the SF-surface, i.e. the surface obtained after the application of the S-filter and the F-operator (thus not applying the L-filter). This is not applied to the profiles, for the adoption of Rv is reported in literature and considered a benchmark.

2.4. Fatigue tests and fractography

All 4PB fatigue tests were carried out on an INSTRON E10000 having a load capacity of 10 kN. The tests were performed at a stress ratio R = 0.1 with a test frequency of approximately 30–35 Hz. The run-out condition was set to 10^7 cycles, while the failure condition corresponds to a stiffness drop of 10%.

For the scope of this project, that looks for a correlation between surface features and fatigue properties, the 4PB specimen geometry was selected to avoid geometrical stress concentrations and to maximize the stressed region.

Comparing with the literature, Beretta et al. [19] adopted 3PB specimens. These specimens have a limited zone subjected to maximum stress, which can be estimated of about $S_{90\%} = 3.6 \times 6 \approx 21\,\text{mm}^2$ considering the area subjected to at least 90% of the maximum applied stress.

Nicoletto [62,63] proposed a 3PB miniature specimen geometry for L-PBF Ti-6Al-4V specimens, which enabled highlighting a significant effect of specimen orientation. The total length of the specimen is only 22 mm, with the aim of maximizing the material saving. In this case, the highly stressed area is reduced to $S_{90\%} \approx 5 \times 1 \approx 5\,\text{mm}^2$.

Narra et al. [64] adopted a 4PB test configuration for the qualification of L-PBF Ti-6Al-4V miniature samples with varying anomaly populations. Such 4PB test configuration consists of two force-rollers with 10 mm span and two pin-rollers with 30 mm span. The total length of the specimen is 35 mm, with $S_{90\%} = 12 \times 5 = 60\,\text{mm}^2$.

The test setup adopted in the present work kept the force rollers' span at the value of 10 mm, but the span of the pin-rollers was doubled at 60 mm. With such an arrangement (similar to the one adopted in [65]), the highly stressed area reaches $S_{90\%} = 15 \times 5 = 75\,\text{mm}^2$.

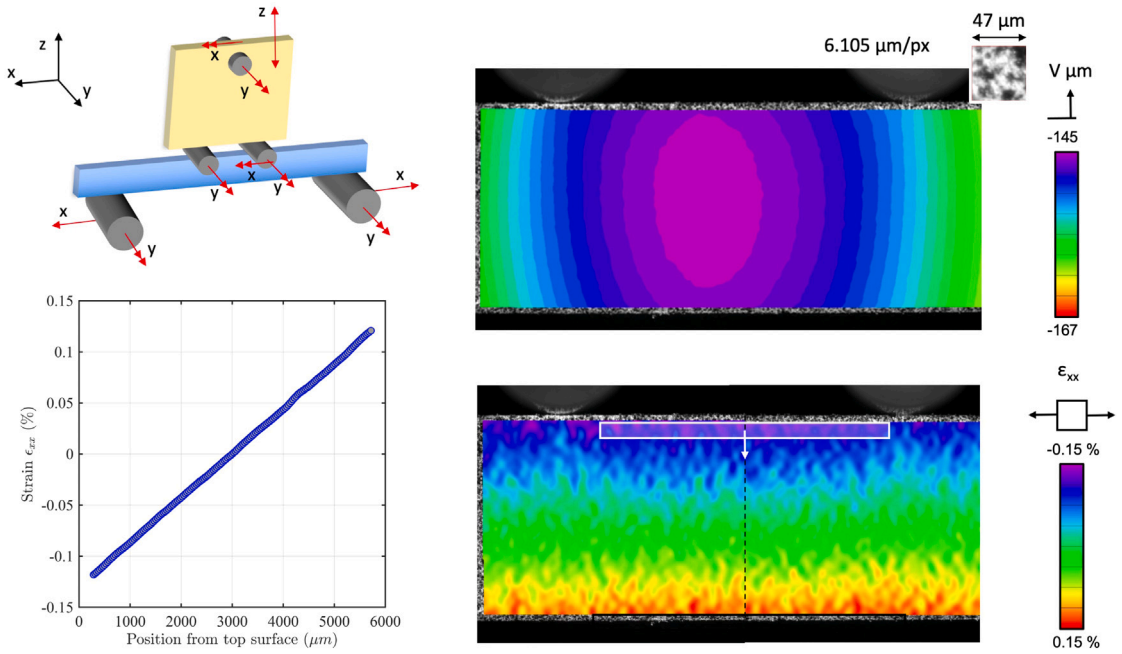

Fig. 4. The 4-point bending set-up schematic indicates the free displacements (single-headed arrows) and the rotations (double-headed arrows) which guarantee the load alignment and the symmetric specimen loading; the experimental vertical displacement and bending strain maps obtained via DIC measurements demonstrate the symmetric specimen deformation and also demonstrate the correct stress calculation.

The 4PB configuration is not isostatic and it is therefore very sensitive to specimen tolerances: initial trials showed that the stress distribution is not symmetrical, if special arrangements are not adopted. Therefore, a special 4PB device was adopted (MTS 642.05A-02 bend fixtures) that allows the top pins to rotate around the proper axis and, additionally, rotate out of the main bending plane to guarantee a perfect alignment and a symmetric specimen loading. A series of tests with digital image correlation (DIC) allowed verifying the linearity of stresses vs. applied load with this arrangement (see Fig. 4).

2.4.1. Fractography

Specimens after the fatigue tests were broken under liquid nitrogen and the fracture surfaces were observed under a Scanning Electron Microscopy (SEM, Zeiss EVO15, equipped with Secondary Electrons, SE, and High Contrast Back Scattered electron, HCBSE, detectors; operated at 20 KV with a working distance of 8.5 mm) to reveal the anomalies at the origin of the failures. Measurements of the anomaly size were taken in terms of $\sqrt{\text{area}}$ parameter proposed by Murakami [59], whose application to surface features was discussed in [19,21,52].

3. Results

3.1. Topography characterization

Fig. 5 shows the surfaces analysed via CSI. H surfaces present a narrow range with large features. Conversely, the height range increases as gravity becomes more and more dominant, and the feature size significantly decreases. Qualitatively, the V surface presents traces of the layers as valleys across the shorter side of the surface.

Surface parameters have been evaluated according to the methodology described in Section 2.3. Figs. 6 and A.16 show the results, highlighting the effect of building condition. Pairwise non-parametric hypothesis testing, to dispense with non-trivial distributional assumption, is performed to test for equality of median at 95% confidence level, with a Mood's median test [66]. As it can be appreciated, the effect of build angle results in an increasingly rougher surface in terms of all considered parameters, even though the most critical increase is provided by the downskin surface. More progressive growth in the increase of roughness is well captured by the Sdq (see Appendix), consistently with its definition.

Contouring effect can be appreciated when comparing H and H_{nc}, for upskin surface, and D and D_{nc}, for downskin. For upskin, no statistically significant changes can be appreciated. Conversely, for downskin, the presence of contouring, which is what is actually measured for a highly sloped downskin surface is statistically appreciated. In particular, lack of contouring (D_{nc}) generates a surface more random (Ssk ~ 0 and Sku ~ 3) and with deeper valleys, which might be liable for reduced fatigue life. This specific result is consistent with the interaction of the building strategy, i.e. the contouring, with the considered downskin surface. In fact, what is actually measured in the downskin geometrical configuration is the contouring effect, i.e. the perimeter of the raster-scanned areas. Contour, when is present (series D), reduces the distance (from a topographical point of view) between layers by remelting the perimeters and thus smoothing the transition hence resulting in shallower valleys.

The effect of measuring instruments and filtering is reported in Fig. 7. As it can be appreciated considering the same length scale of a roughness profile (i.e., CSI profile, μ-XCT profile and the stylus thus evaluating Rv) and of SL-surface (i.e., CSI-SL and μ-XCT-SL thus evaluating Sv) Rv evaluated from profiles is systematically underestimating the valley depth. This is the result of a superimposition of two effects, i.e., the worse representativeness of a profile measurement and the mechanical convolution of the stylus with the surface introducing a further filtering on the surface. The latter effect, which is ultimately tied to the lateral resolution, is particularly appreciable considering the profilometry measurements only. In fact, CSI results in a higher Rv thanks to the better resolution. Such resolution effect can also be seen considering at the same length scale topographical measurement by CSI and μ-XCT. The CSI having better resolution (~ 3 µm lateral and 1 nm vertical) can measure deeper and steeper features that μ-XCT (with a voxel size of ~ 12.5 µm).

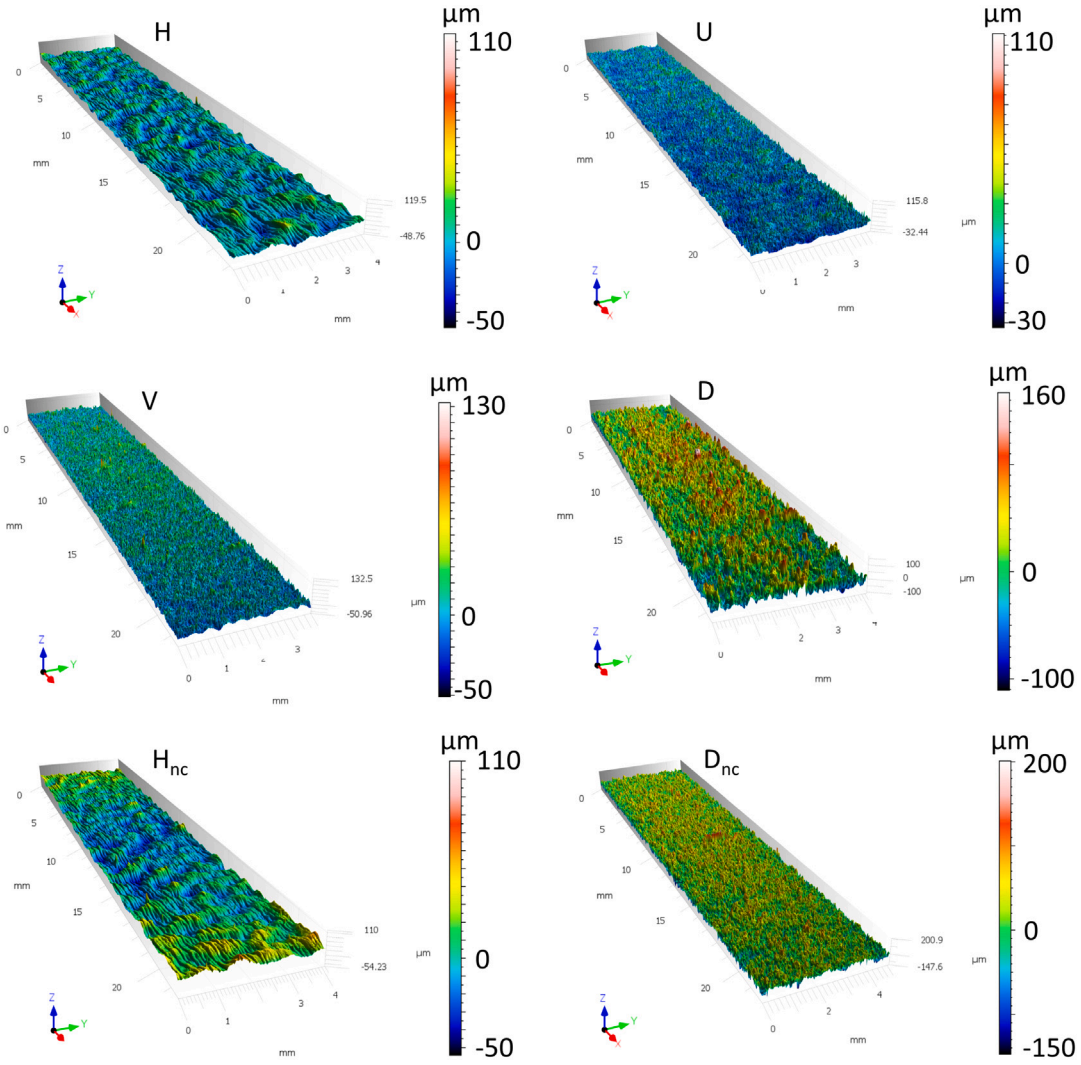

Fig. 5. Measured surface topographies of the considered specimens. One sample per series is shown.

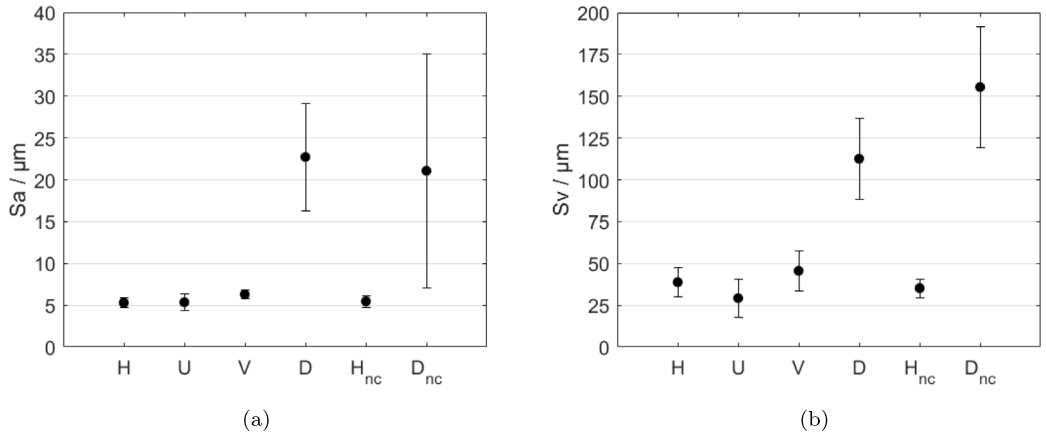

Fig. 6. Comparison of the evaluated topographical parameters on the CSI-measured surfaces depending on the building angle: (a) areal arithmetic mean deviation Sa, (b) areal maximum valley depth Sv. Other parameters are reported in Appendix.

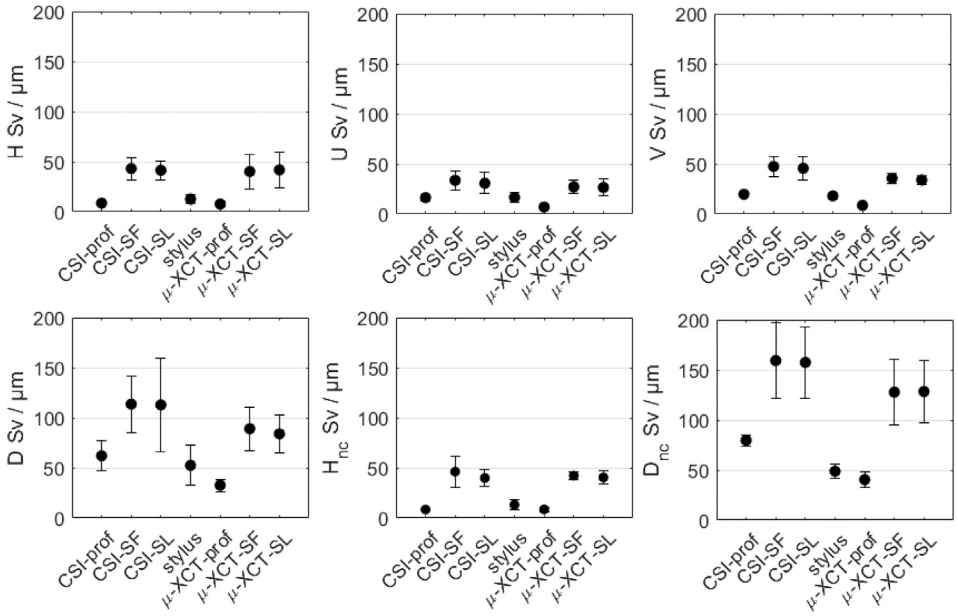

Fig. 7. Comparison of the effect of measuring instrument and filtering on maximum valley depth.

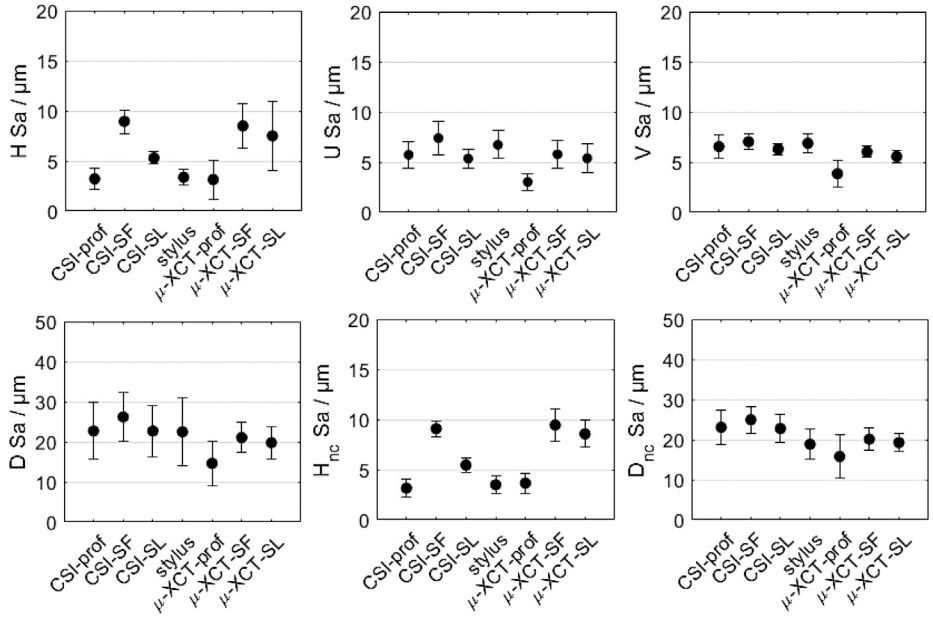

Fig. 8. Comparison of the effect of measuring instrument and filtering on average height.

Coming to the effect of filtering, given the same instrument (CSI or μ-XCT), as per literature and as expected, SL-surface Sv is systematically smaller than SF-Surface Sv. This is due to the removal of additional topographical larger scales components. Complementary results are reported in terms of Sa in Fig. 8, in which case less evident changes can be appreciated thanks to its robustness. Additional results are reported in terms of Sq and of Rsm in Appendix.

3.2. Detection of crack locations

After fatigue testing, crack initiation location was evaluated and the surface feature at the origin of fatigue failure was identified. Some coupons highlighted the presence of multiple surface cracks, as depicted in Fig. 9.b. The features of interest were then identified in the reconstructions of coupons scanned before tests. In most cases, little visual change was observed but cracks could be easily correlated to the deepest surface depressions, as is clearly visible in Fig. 9.c.

3.3. Fatigue test results

Following the same methodology of ASTM E739 [67], the JSME standard method [68] with small sample number was adopted for the analysis of the finite-life part of the S-N curve of each series, that is

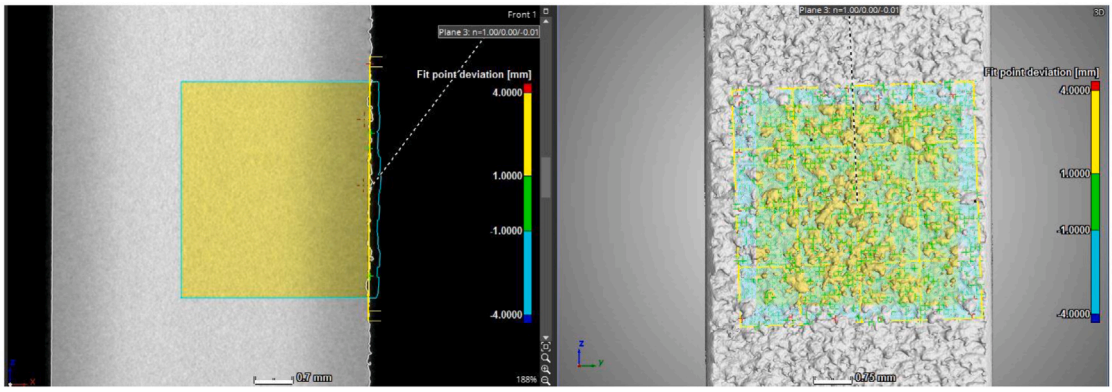

(a)

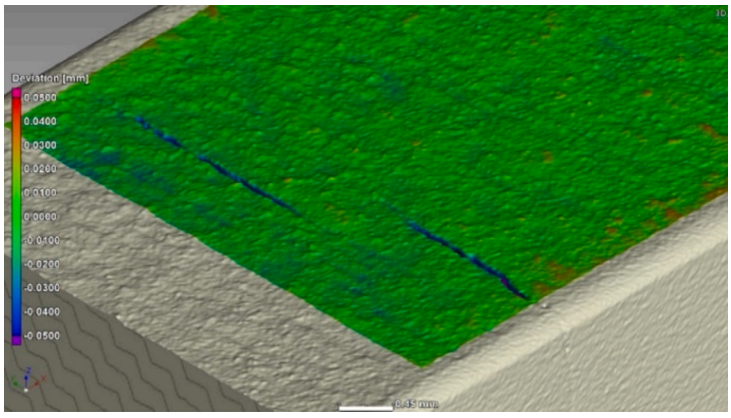

(b)

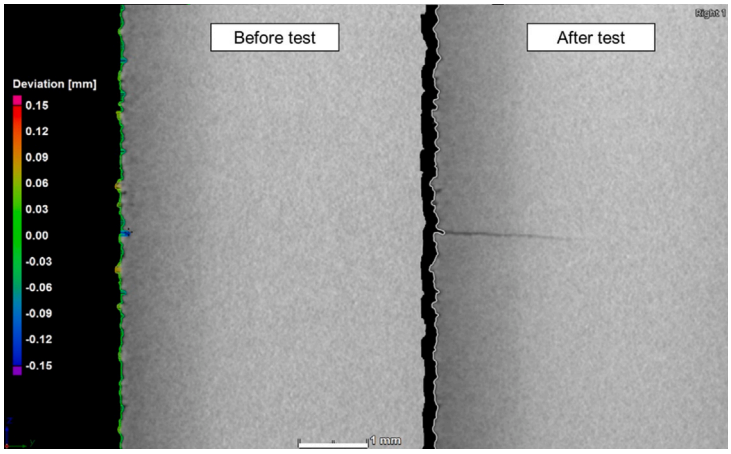

(c)

Fig. 9. Details of μ-XCT investigation: (a) definition of region of interest and reference plane for roughness analysis; (b) evidence of multiple cracks on one U specimen; (c) comparison of μ-XCT image before and after fatigue testing on one D_{nc} specimen showing that crack nucleated from deepest surface intrusion detected before test.

described by the following relationship:

$$\Delta\sigma = C \cdot N^{-b} \tag{1}$$

where the constants C and b are the outcome of the regression with the least-squares method.

Hodge–Rosenblatt's up and down method with a short stair-case sequence [69] of 6 specimens was used as prescribed in [68] to estimate the fatigue limit. A 50% failure probability is computed as the average of stair-case experimental results of the fatigue tests. Failures in the stair-case region were not included in the fit of the finite life region.

The specimens that went run-out were retested at a higher stress range to obtain fracture surfaces to be checked at the SEM. The measurements of the surface features at the origin of the failures (discussed in Section 3.4) is shown in Fig. 10.b.

The S-N curves of the various series are shown in Fig. 10.a, normalized by the endurance limit of the machined series. Failures are represented by cross-markers and run-outs by empty triangles; the regression curve of the fatigue data at the 50% failure probability is a solid-coloured line.

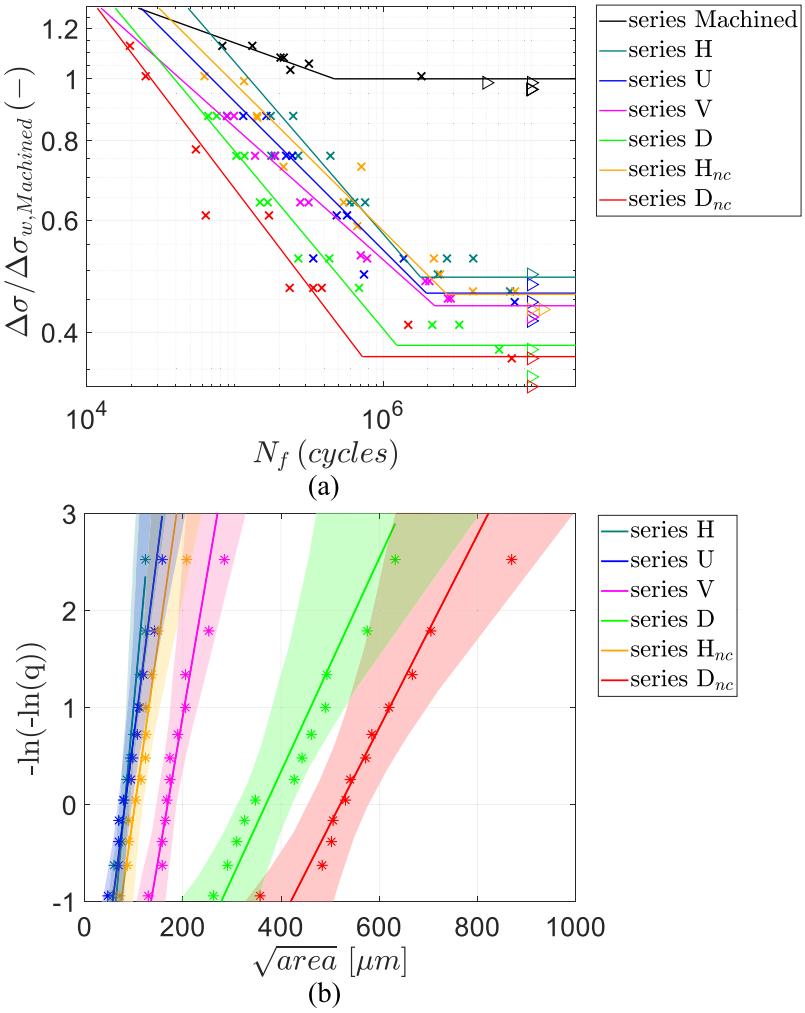

Fig. 10. Fatigue test results for the L-PBF Co–Cr–Mo alloy: (a) Comparison of S-N curves normalized with respect to the endurance limit of the machined series; (b) Largest extreme value distribution (LEVD) probability plot of the size of the anomaly at the origin of failure for the as-built series.

Table 3
Parameters of the S-N curves of all the tested series: slope of the finite-life region b, normalized experimental fatigue limit $\Delta\sigma_f/\Delta\sigma_{f,M}$ and number of cycles at the knee-point N_{lim}.

Series	b	$\Delta\sigma_f/\Delta\sigma_{f,M}$	N_{lim} [cycles]
M	0.084	1.00	$4.69 \cdot 10^5$
H	0.27	0.49	$1.79 \cdot 10^6$
U	0.23	0.46	$1.96 \cdot 10^6$
V	0.21	0.44	$2.24 \cdot 10^6$
D	0.28	0.38	$1.24 \cdot 10^6$
H_{nc}	0.23	0.46	$2.71 \cdot 10^6$
D_{nc}	0.31	0.37	$7.25 \cdot 10^5$

A summary of all the parameters of the S-N curves is displayed in Table 3:

- $\Delta\sigma_e$ is the normalized endurance limit at 10^7 cycles for the 4PB tests at R = 0.1;
- N_{lim} is the number of cycles at the knee point of the S-N curve at the endurance limit.

3.4. Analysis of fractures and surface anomalies

The main anomaly types observed at the fracture origin are depicted in Fig. 11. No sub-surface or internal anomalies were found at the fracture origin. The criteria adopted to measure anomaly size are summarized below.

- **Grains:** This is an anomaly typical for the horizontal series H and H_{nc} (smooth surface, Fig. 11.a) and, sometimes, for vertical and upskin series (waved surfaces, Fig. 11.b). In these latter cases such anomalous grains are localized at the bottom of surface valleys generated by the building process. In the case aggregates of weak grains are present at the fracture origin, the anomaly size is taken as square root of the weak grain region area on the fracture plane (see Fig. 12.a). The weak grain region is selected by visual analysis of the grey intensity variations on the SEM image;
- **Intrusion**: a deep surface depression (width w much smaller than depth t). In the case a surface intrusion is present at the fracture origin (see Fig. 11.c);
- **Groove:** this is a shallow and elongated crack initiation zone on the surface (Fig. 11.d) where the inherent surface roughness (one large and shallow surface depression or a series of valleys) can be considered as an elongated anomaly with large width-to-depth ratio w/t (see Fig. 12.b).

Intrusions and grooves are found randomly on the fracture surfaces of the U, V series and frequently, and with pronounced sizes, on the fracture surfaces of rough D and D_{nc} series.

According to Murakami [59], the fatigue failure depends on the driving force of the failure-leading crack, i.e., on the Stress Intensity

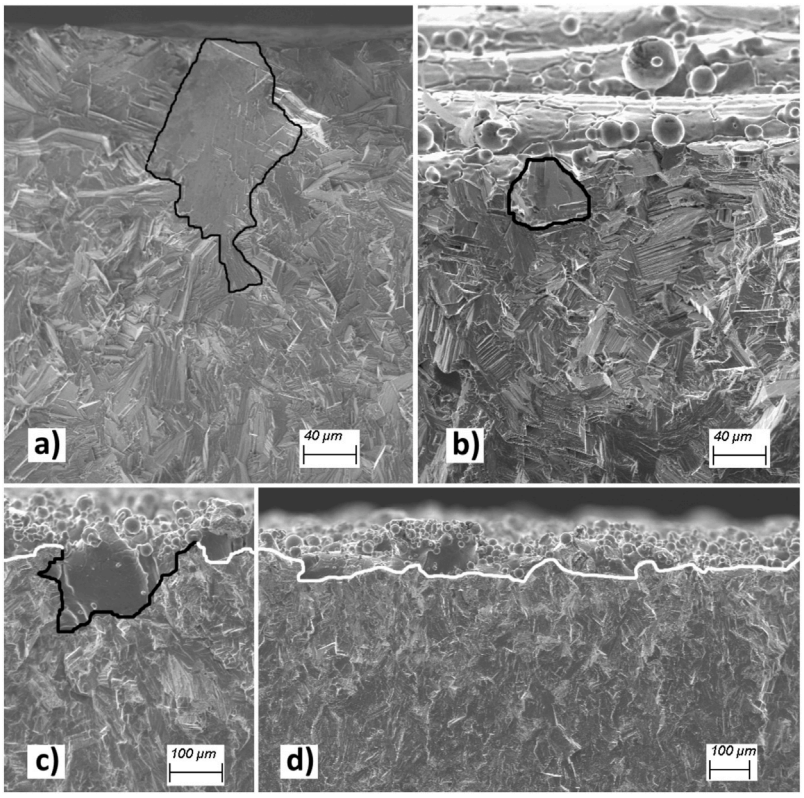

Fig. 11. SEM observations of typical anomalies: (a) anomalous grain in smooth horizontal H series; (b) anomalous grain at the valley of series upskin 45° U; (c) deep intrusion in downskin 135° D series; (d) groove in downskin non-contour D_{nc} series.

Factor (SIF) that can be easily calculated through the $\sqrt{\text{area}}$ parameter. By defining the anomaly thickness t and width w, $\sqrt{\text{area}}$ can be simply estimated as:

- square root of the projected area of a 3D anomaly on a plane perpendicular to the loading direction, if $w/t < 10$;
- $\sqrt{10 \cdot t}$ for elongated anomalies or surface grooves ($w/t > 10$) (e.g., this is the typical configuration for surface grooves in D and V series, see Fig. 11).

The anomaly depth on the SEM images of the fracture surfaces is measured as described in [52]. In details, the position of the reference line is determined by first identifying the highest protrusion in the crack initiation zone, and then shifting the line starting from the peak of the protrusion through the centre of the specimen of the amount R_{pm} (mean profile peak height). This process allows setting the reference line so that the height of protrusions and attached particles, that do not induce any stress concentration or singularity, are not measured as part of the *initial anomaly* (see Fig. 12.b). The R_{pm} profile roughness parameter used to position the horizontal reference line on the SEM fractography image is averaged over all the profiles from CSI surface topographies of all the specimens of a series. The profile measurement methodology is described in Section 2.3.

The Gumbel (or LEVD) distribution is suitable to describe the size distribution for anomalies at the failure origin in terms of $\sqrt{\text{area}}$ and it has shown to be applicable also to surface features [21]. The cumulative density function (F) of the anomaly size is defined by Eq. (2):

$$F(\sqrt{\text{area}}) = \exp\left\{-\exp\left[-\frac{\left(\sqrt{\text{area}} - \lambda\right)}{\delta}\right]\right\} \quad (2)$$

Table 4
Parameters of the LEVD of anomaly size at fracture origin for all the tested series.

Series	δ [μm]	λ [μm]	μ [μm]	σ [μm]
H	18.0	81.7	92.1	23.1
U	25.4	82.6	97.2	32.6
V	33.8	169.1	188.7	43.4
D	90.9	369.2	421.6	116.6
H_{nc}	28.3	102.6	118.9	36.3
D_{nc}	100.6	520.4	578.4	129.0

whose parameters are the *location* parameter λ (which is the modal value of the distribution) and the *scale* parameter δ.

This distribution statistically describes a population obtained from a Block Maxima sampling, i.e., where only the maximum values have been sampled [70]. This is the case for the surface features of 4PB specimens, as the stress is uniform in the central region, so the most detrimental feature over this area acts as preferential crack initiation location.

Fig. 10.b shows the LEVD distributions interpolating the anomaly size at the origin of failure for each series: data are plotted on Gumbel probability plots (the λ parameter corresponds to a y-axis value of 0). As it can be seen, the slope of the lines (which is related to the data dispersion) is quite similar for all the sample orientations except for series D and D_{nc}, which correspond to the largest anomalies. There is a clear trend of increasing defect sizes from series H to D: it evidences a significant correlation between the size of critical surface anomalies and fatigue strength (see Table 4).

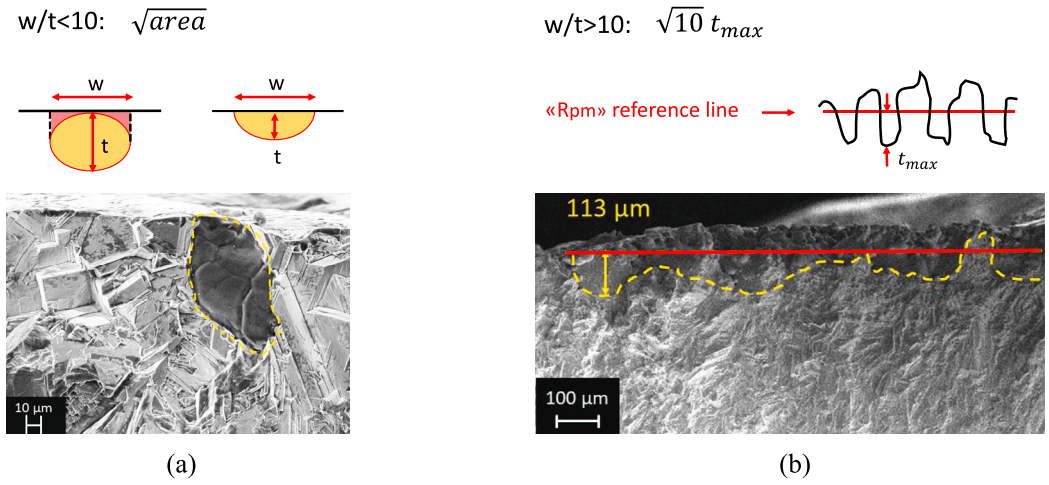

Fig. 12. Measurement method for the size of the anomalies at the failure origin on SEM images of the fracture surface. The crack size equivalent to an anomaly with aspect ratio: (a) $w/t < 10$ is $\sqrt{\text{area}}$ (example: anomalous grain /grain aggregates or intrusion); (b) $w/t > 10$ is $\sqrt{10}t_{max}$ with w =anomaly width, t =anomaly depth, t_{max} max depth of the grooves (example: surface grooves).

4. Analysis of results

4.1. Modelling of fatigue strength

It is widely accepted that modelling the short crack effect supports the endurance limit prediction of AM parts [71–74]. To this aim, the El-Haddad model [75] is utilized in this study to consider the short-crack effect for the endurance limit $\Delta\sigma_w$:

$$\Delta\sigma_w = \Delta\sigma_{w,0}\sqrt{\frac{\sqrt{\text{area}_0}}{\sqrt{\text{area}}+\sqrt{\text{area}_0}}} \tag{3}$$

$$\sqrt{\text{area}_0} = \frac{1}{\pi}\left(\frac{\Delta K_{\text{th,LC}}}{Y\cdot\Delta\sigma_{w,0}}\right)^2 \tag{4}$$

where $\Delta\sigma_{w,0}$ is the endurance limit stress range for anomaly-free material, $\sqrt{\text{area}_0}$ is the El-Haddad size parameter, and $\Delta K_{\text{th,LC}}$ is the long crack SIF threshold range. Based on Eqs. (3) and (4), the El-Haddad model requires two material parameters to be determined. Based on previous Company test results on $\Delta K_{\text{th,LC}}$ and $\Delta\sigma_{w,0}$ for the present Co–Cr–Mo alloy, the $\sqrt{\text{area}_0}$ parameter was expected to be relatively large (≈ 250 µm).

Artificially micro-notched specimens were tested to get experimental confirmation of short cracks behaviour. A rectangular notch geometry with dimensions of 0.1 mm depth and 0.3 mm superficial length was selected, equivalent to an anomaly size of $\sqrt{\text{area}}$ = 173 µm. Providing $\Delta K_{\text{th,LC}}$ and the endurance limit measured on notched specimens $\Delta\sigma_{w,\left(\sqrt{\text{area}}=173\mu m\right)}$, Eq. (3) was then fitted considering the anomaly-free endurance limit $\Delta\sigma_{w,0}$ as a fitting parameter.

The fatigue test results are summarized in Fig. 13 including the El-Haddad model and the endurance limit obtained with the micro-notched fatigue specimens used to fit it (yellow-filled circular dot), $\Delta\sigma_{w,\left(\sqrt{\text{area}}=173\mu m\right)}$. The failures are indicated with crosses, while run-outs are indicated with circular dots. The horizontal position of all data points was based on the equivalent anomaly size $\sqrt{\text{area}}$ measured on the fracture surfaces.

The fatigue test results indicate that the El-Haddad model properly describes the endurance limit region for the present Co–Cr–Mo alloy, and it is able to describe the effect of the surface anomalies in the different test series.

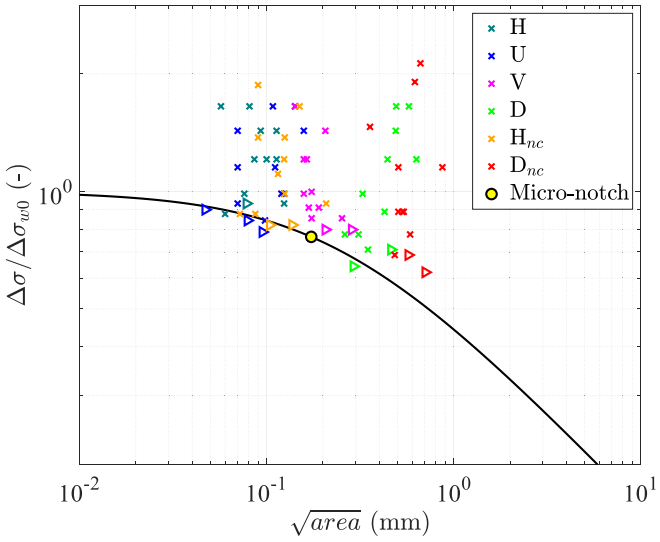

Fig. 13. Fatigue test results compared with El-Haddad model (crosses represent failures, while triangles are run-outs).

4.2. Comparison of measurements with anomalies at the origin of failure

The LEVDs of the maximum anomaly size/valley per specimen are adopted to compare the surface measurements and the initial flaw size detected on the fracture surfaces of the various series. The comparison is based on the mean value and the bounds at a 95% unilateral confidence at a fixed percentile. Fig. 14 shows the error bars of the various series of specimens at the 50% percentile, where the confidence bounds of the fractographic measurement are taken as reference and displayed as a shaded region.

The results for CSI and μ-XCT refer to Sv evaluated on SF-surfaces to avoid any impact of filtering on the anomaly size estimations, considering the reasonable assumption that filtering removes relevant components in the size estimation of anomalies at the origin of fatigue failure; as per contact stylus results, Rv is considered. Comparisons are made in terms of $\sqrt{\text{area}}$. The 50% percentile of valley depth LEVD

distributions ($t_{50} = Rv_{50}$ or Sv_{50}) are converted to $\sqrt{\text{area}}$ using Eq. (5) for calculating the prospective average size for shallow surface defects.

$$\sqrt{\text{area}}_{50} = \sqrt{10} \cdot t_{50} \tag{5}$$

The error-bars are compared to the fractography data: whenever they are included in the shaded bands, the surface measurements are deemed to precisely estimate size of the anomaly originating fatigue failure.

Regardless of the measurement method, a clear ranking of the as-built series emerges from the visual analysis of the error bars in Fig. 14.a (data are reported in Table A.6): downskin orientation is the most critical for fatigue, having the largest anomaly size among the series; conversely, the H-series and U-series appear less critical. The V-series has an intermediate anomaly size between the best and the worst surface qualities. A beneficial effect of the contour is seen when comparing the D-series, as D is associated to slightly smaller size than D_{nc}.

Comparing the different measurement methods (easier visualization is provided in Fig. 14.b by normalization of percentile bands with respect to the average of fractography measurements), it can be observed that the stylus does not superimpose with the other methods and largely underestimates the anomaly size. Moreover, there is a systematic difference between the fractography bands and the estimates from areal measurements with μ-XCT and CSI, except for series U, for which the bands are superimposed. The lack of accuracy of stylus estimates can be due to two reasons: (i) the mechanical filter of the stylus's tip, which is unable to capture the narrow depressions [31]; (ii) the fact that 1D measurements sample less area than areal ones.

"μ-XCT-SF" systematically underestimates anomaly size as compared to CSI, perhaps due to the lower resolution of the sampled topography.

As far as the comparison between fractography and areal surface measurements is concerned, the systematic underestimation that is shown in Fig. 14 justifies the claim of dispensing waviness filtering to avoid the addition of further Sv reduced evaluation. In fact, as it has been shown in Section 3.1, the characterization of an SL-surface yields an underestimation of topographical parameters with respect to the SF-surface.

There is an intersection between the bands of fractography and areal "CSI-SF" roughness estimates for most series and the systematic differences between the areal CSI-SF roughness estimates consist of just slight underestimations for the roughest series, i.e. V, D, D_{nc}, which justifies the claim of dispensing waviness filtering to avoid the addition of further Sv reduced evaluation, as it has been shown in Section 3.1 and recalled above.

Oppositely, the differences are most severe in the case of H-series. This is also true for μ-XCT-SF estimates. For the H-series, the overestimation is caused by the aspect ratio, as the approximation on anomaly size introduced via Eq. (5) is only applicable to shallow anomalies, while it conservatively overestimates the area in the presence of grains/intrusions anomalies.

The comparison between estimated anomaly size and fractographic measurements is shown in Table 5 in terms of average values. It can be seen that the maximum error for CSI is of the order of 20%.

4.3. Fatigue strength prediction from roughness measurements

The predictions for fatigue strength based on the anomaly sizes estimated by CSI roughness measurements and Eq. (3) are shown in Fig. 15, considering on the 2.5%, 50% and 97.5% percentiles of their LEVD distributions. The experimental and estimated endurance limits are reported normalized with respect to $\Delta\sigma_{w0}$.

As evident from the results, the predictions demonstrate a relatively good level of accuracy, as they successfully capture the overall trend and exhibit overlapping of the scatter bands with the theoretical line and its 2.5 – 97.5% scatter band (calculated by averaging the scatter of the fatigue limit across different series). However, it is worth noting that a statistically significant difference is observed only for series H. This difference can be attributed to the conservative estimation

Table 5
Errors (%) of the estimates of anomaly $\sqrt{\text{area}}$ at the origin of fatigue failures with respect to fractography. Bold green values represent estimates consistent with fractography, while red ones are significantly different.

Series	CSI-SF	μ-XCT-SF	Stylus
H	47	45	−56
U	9	−6	−44
V	−21	−38	−69
D	−15	−30	−60
H_{nc}	21	19	−64
D_{nc}	−14	−27	−73

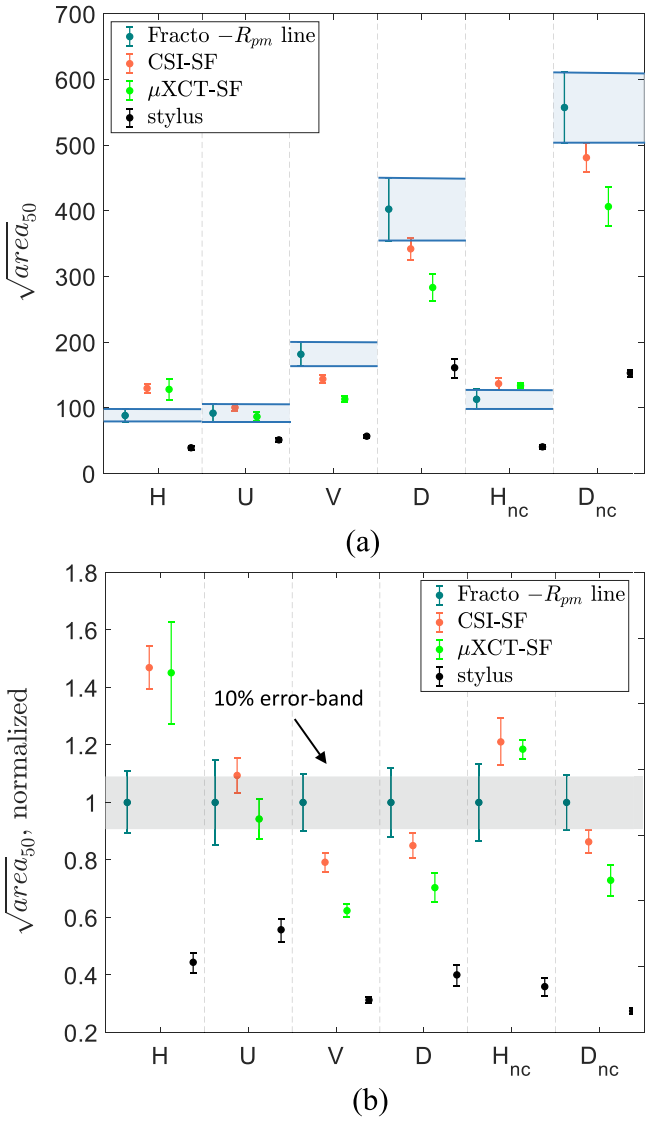

Fig. 14. Comparison between the anomaly size from fractography and the surface measurements in terms of the 50% percentile $\sqrt{area_{50}}$ from the LEVD of the areal measurements (distribution of maxima: 1 maximum per specimen/surface): (a) comparison of the $\sqrt{area_{50}}$ bands for the different as-built series (the fractography-based bands are the reference shaded region); (b) $\sqrt{area_{50}}$ bands for the different series normalized with respect to the fractography $\sqrt{area_{50}}$; a shaded region representing the 10% error with respect to the unity is depicted.

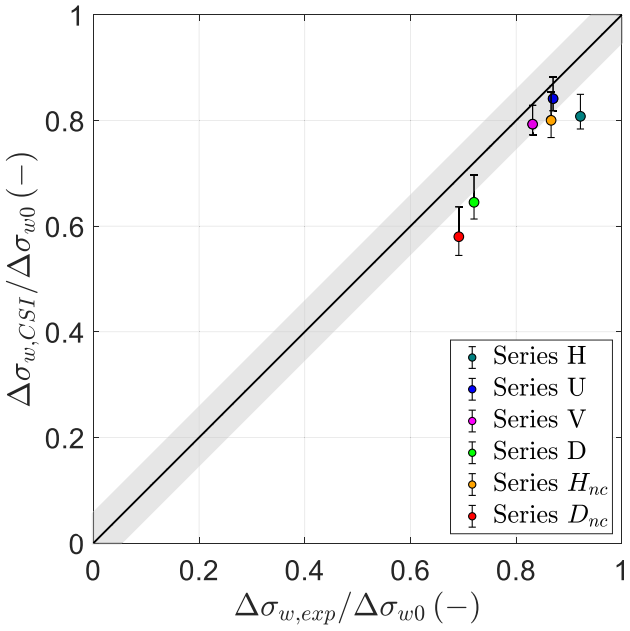

Fig. 15. Fatigue strength predictions for the different series estimated by Eq. (3) and the anomaly sizes estimated by CSI roughness measurements.

of defect size using Eq. (5) assuming the defects to be grooves, an assumption surely conservative for the actual shape of defects detected on horizontal specimens.

The conclusion that can be drawn is that the roughness measurements can be adopted for a *local* assessment of the surface quality of a L-PBF part by comparing the estimated anomaly size with an allowable calculated with deterministic safety factor or probabilistic analyses [76].

5. Conclusions

This study explored the correlation between surface quality and fatigue strength of Co–Cr–Mo alloy produced through L-PFB, considering orientation and contouring parameters. The objective is to develop a straightforward yet reliable method for estimating the fatigue strength of various surface states using non-destructive measurements.

The main conclusions of this research are summarized below:

- Newly designed 4PB specimens proved to be an excellent option to perform low-cost and rapid screening on surface fatigue strength and distinguish different surface states. The use of these specimens reduces powder requirements and space on the platform compared to conventional fatigue coupons. Manufacturing along any orientation becomes straightforward, and non-destructive inspections are simplified thanks to the small specimen volume and flat surface of interest.
- Downskin specimens provided the lowest fatigue strength, with a debit around 60% in the HCF region as compared to machined coupons. Horizontal and upskin orientations showed the best strength, with approximately a 20% improvement with respect to the downskin. Vertical orientation fell in the middle.
- Contouring slightly improved fatigue strength independently on the orientation.
- Different anomaly type and shape were found at the origin of failure depending on the orientation: high quality surfaces (horizontal, upskin) showed grain aggregates or intrusions well described by a semi-elliptical shape, while rougher surfaces (vertical and downskin) presented elongated grooves.
- μ-XCT performed before and after fatigue tests demonstrated that fatigue failures were originated from deep valleys, and that the maximum valley depth would be a good indicator of expected surface fatigue strength;
- Fracture mechanics-based methods including a short cracks approach provided a robust estimation of fatigue strength in HCF based on anomaly size evaluated via $\sqrt{\text{area}}$ parameter. Maximum valley depth can conservative be adopted to estimate the maximum anomaly size considering anomalies elongated on the surface.
- Contact 1D measurements (stylus) provided similar qualitative trends as non-contact 2D ones (CSI), but proved largely non-conservative in determining the maximum valley depth. Roughness calculation via μ-XCT provided reasonably good results, better than stylus, but less accurate than CSI.
- Good correlation was identified between Sv parameter measured via CSI and the anomaly sizes estimated with $\sqrt{area} = \sqrt{10} \cdot S_v$.

Considering the aforementioned factors, it can be concluded that a precise estimation of fatigue strength for a generic surface quality in additive manufacturing can be achieved through a combination of high-quality non-destructive roughness measurements, statistical analysis, and fracture mechanics-based assessments. This approach ensures a reliable evaluation that paves the way for optimizing and enhancing the performance of additive manufactured components. Additionally, this would provide the capability of comparing different surface states and selecting the best option for fatigue strength with limited experimental effort, e.g., during parameter optimization, selection of most suitable surface improvement techniques, or to verify process stability. Finally, the method could set a basis for part design or life calculation dependent on actual surface orientation, which could be a possible input for future applications of probabilistic approaches.

Declaration of competing interest

The authors declare the following financial interests/personal relationships which may be considered as potential competing interests: Simone Romano reports financial support was provided by Government of Italy Ministry of Economic Development.

Data availability

The authors do not have permission to share data.

Acknowledgements

This research has been conducted as a collaboration of GE Avio, Politecnico di Milano, and Politecnico di Torino in the framework of GE Avio's European Technology Development Cluster (E-TDC) on Additive Manufacturing. GE Avio acknowledges funding by Italian Ministry with the contract CdS 605 CUP C97I17000990008. The authors want to thank Prof. Anton Du Plessis, Muofhe Tshibalanganda, and Carlyn M. Wells from Stellenbosch University for their support in performing X-ray CT scans, reconstructions, and analyses.

Appendix

See Figs. A.16–A.18 and Table A.6.

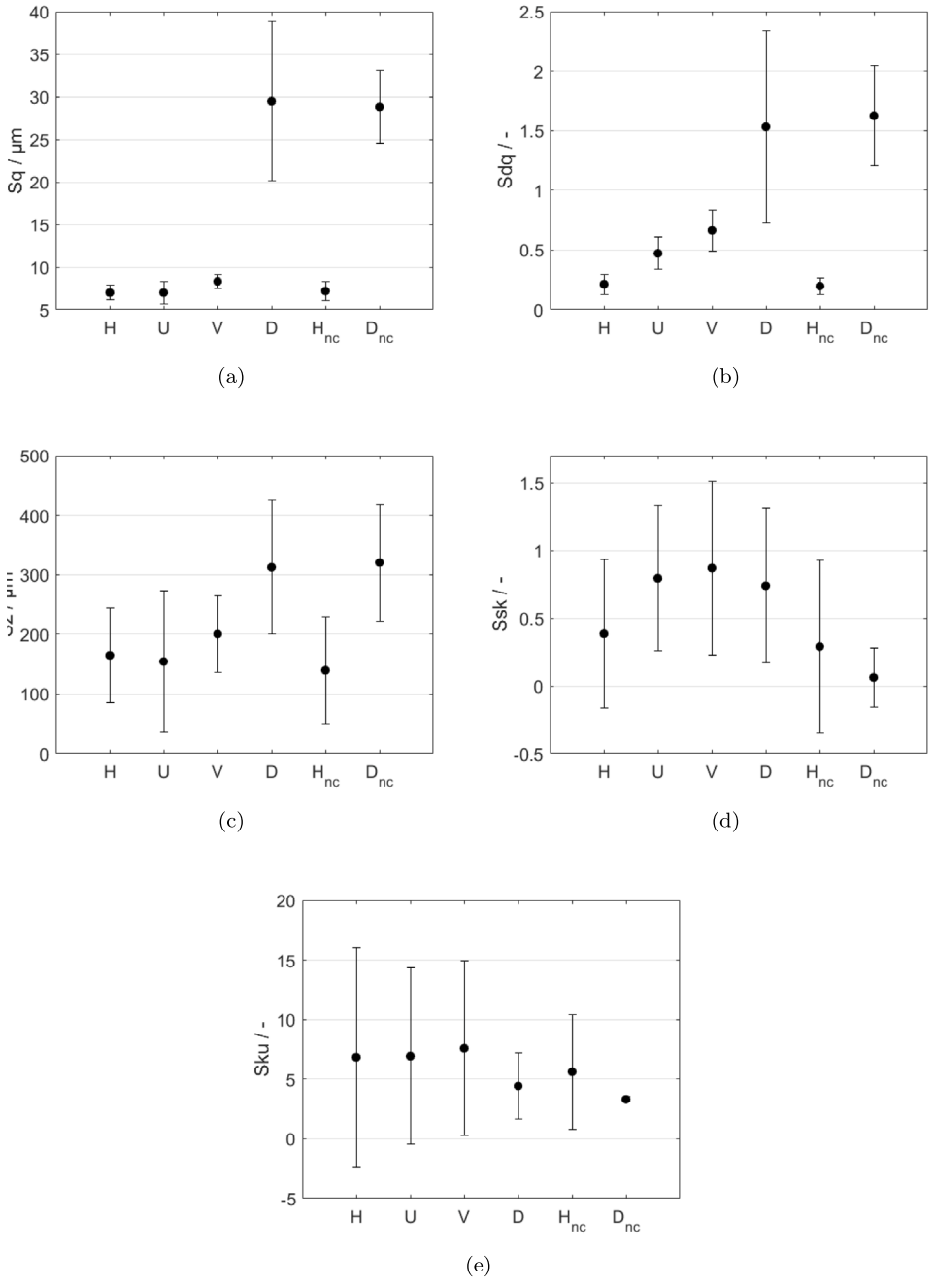

Fig. A.16. Comparison of the evaluated topographical parameters on the CSI-measured surfaces depending on the building angle: (a) Sq, (b) Sdq, (c) Sz, (d) Ssk, (e) Sku.

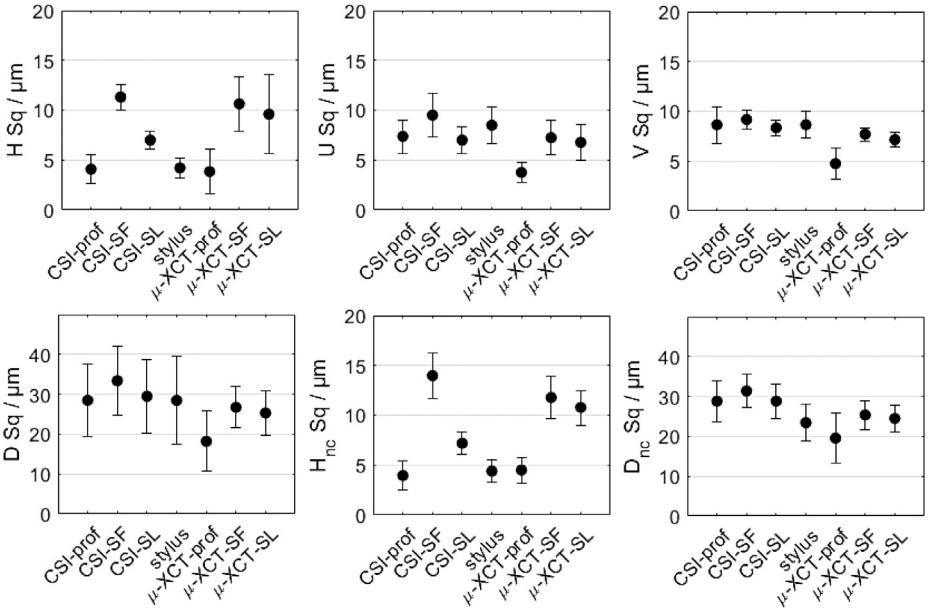

Fig. A.17. Comparison of the effect of measuring instrument and filtering on root mean square height.

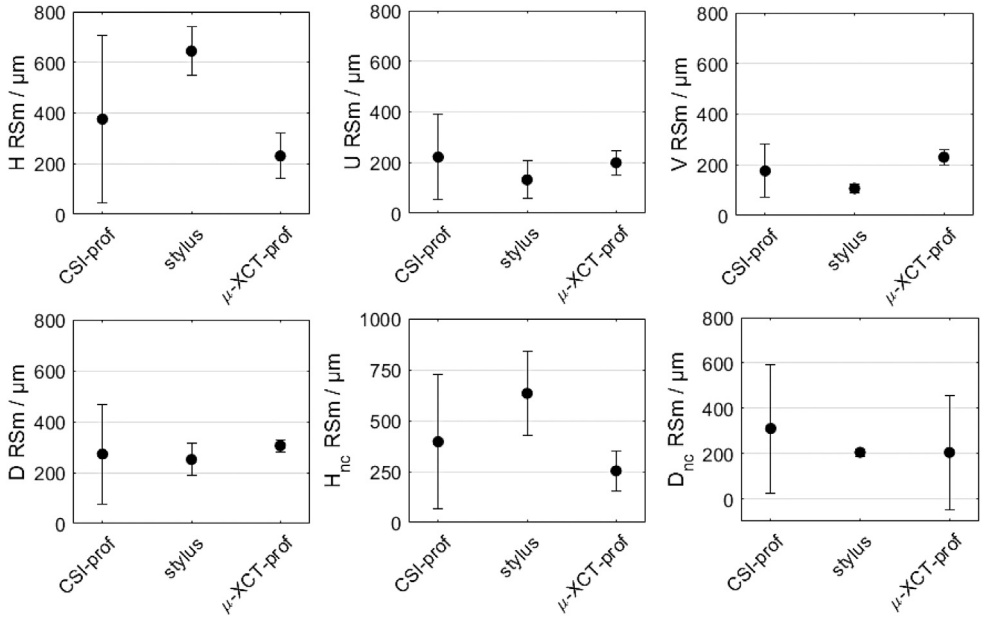

Fig. A.18. Comparison of the effect of measuring instrument and filtering on spacing parameter RSm. This parameter is instrumental to $\sqrt{\text{area}}$ and F computations. Literature defined relationship using this parameter for shielding. Because it is native and specific to profile characterization, its evaluation of surface requires undersampling by profiles extraction.

Table A.6
Comparison between fractography anomaly size ($\sqrt{\text{area}}$), and the estimated size by CSI-SF, μ-XCT-Sf and stylus in terms of the 50% percentile with 95% confidence bands.

Series	Fracto $-R_{pm}$	CSI-SF	μ-XCT-SF	Stylus
H	88.3 ± 9.5	129.7 ± 6.7	128.1 ± 15.6	39.2 ± 3.0
U	91.9 ± 13.5	100.5 ± 5.7	86.6 ± 6.5	51.2 ± 3.5
V	181.6 ± 17.9	143.8 ± 6.0	113.2 ± 4.2	56.8 ± 2.0
D	402.5 ± 48.2	342.1 ± 17.0	283.2 ± 19.8	161.1 ± 15.0
H_{nc}	113.0 ± 15.0	136.8 ± 9.2	133.9 ± 3.8	40.6 ± 3.5
D_{nc}	557.2 ± 53.3	480.9 ± 22.5	406.4 ± 30.2	153.0 ± 5.0

References

[1] Seifi M, Gorelik M, Waller J, Hrabe N, Shamsaei N, Daniewicz S, et al. Progress towards metal additive manufacturing standardization to support qualification and certification. Jom 2017;69(3):439–55.

[2] Gorelik M. Additive manufacturing in the context of structural integrity. Int J Fatigue 2017;94:168–77.

[3] Mostafaei A, Zhao C, He Y, Ghiaasiaan SR, Shi B, Shao S, et al. Defects and anomalies in powder bed fusion metal additive manufacturing. Curr Opin Solid State Mater Sci 2022;26(2):100974.

[4] Barari A, Kishawy H, Kaji F, Elbestawi M. On the surface quality of additive manufactured parts. Int J Adv Manuf Technol 2017;89:1969–74.

[5] Mower TM, Long MJ. Mechanical behavior of additive manufactured, powder-bed laser-fused materials. Mater Sci Eng A 2016;651:198–213. http://dx.doi.org/10.1016/j.msea.2015.10.068, URL https://www.sciencedirect.com/science/article/pii/S092150931530530X.

[6] Chan KS. Characterization and analysis of surface notches on Ti-alloy plates fabricated by additive manufacturing techniques. Surf Topogr: Metrol Prop 2015;3(oct):044006.

[7] Townsend A, Senin N, Blunt L, Leach R, Taylor J. Surface texture metrology for metal additive manufacturing: A review. Precis Eng 2016;46:34–47.

[8] Triantaphyllou A, Giusca CL, Macaulay GD, Roerig F, Hoebel M, Leach RK, et al. Surface texture measurement for additive manufacturing. Surf Topogr: Metrol Prop 2015;3(2):024002.

[9] Gockel J, Sheridan L, Koerper B, Whip B. The influence of additive manufacturing processing parameters on surface roughness and fatigue life. Int J Fatigue 2019;124:380–8.

[10] Lee S, Rasoolian B, Silva DF, Pegues JW, Shamsaei N. Surface roughness parameter and modeling for fatigue behavior of additive manufactured parts: A non-destructive data-driven approach. Addit Manuf 2021;46:102094. http://dx.doi.org/10.1016/J.ADDMA.2021.102094.

[11] Cutolo A, Lammens N, Boer KV, Erdelyi H, Schulz M, Muralidharan GK, et al. Fatigue life prediction of a L-PBF component in Ti-6Al-4V using sample data, FE-based simulations and machine learning. Int J Fatigue 2023;167:107276.

[12] Greitemeier D, Dalle Donne C, Syassen F, Eufinger J, Melz T. Effect of surface roughness on fatigue performance of additive manufactured Ti-6Al-4V. Mater Sci Technol 2016;32(7):629–34. http://dx.doi.org/10.1179/1743284715Y.0000000053.

[13] Johannes G, Brandão AD, Emilie B, Thomas R, Tommaso G, Beretta S, et al. Expression of additive manufacturing surface irregularities through a flaw-based assessment. In: STP 1620 on structural integrity of additive manufactured parts. ASTM; 2020, p. 234–49.

[14] Yadollahi A, Mahtabi M, Khalili A, Doude H, Newman Jr J. Fatigue life prediction of additively manufactured material: Effects of surface roughness, defect size, and shape. Fatigue Fract Eng Mater Struct 2018;41(7):1602–14.

[15] Zhang J, Fatemi A. Surface roughness effect on multiaxial fatigue behavior of additive manufactured metals and its modeling. Theor Appl Fract Mech 2019;103:102260.

[16] Solberg K, Guan S, Razavi SMJ, Welo T, Chan KC, Berto F. Fatigue of additively manufactured 316L stainless steel: The influence of porosity and surface roughness. Fatigue Fract Eng Mater Struct 2019;42(9):2043–52.

[17] Nakatani M, Masuo H, Tanaka Y, Murakami Y. Effect of surface roughness on fatigue strength of Ti-6Al-4V alloy manufactured by additive manufacturing. Procedia Struct Integr 2019;19:294–301.

[18] Romano S, Nezhadfar P, Shamsaei N, Seifi M, Beretta S. High cycle fatigue behavior and life prediction for additively manufactured 17-4 PH stainless steel: Effect of sub-surface porosity and surface roughness. Theor Appl Fract Mech 2020;106:102477.

[19] Beretta S, Gargourimotlagh M, Foletti S, du Plessis A, Riccio M. Fatigue strength assessment of “as built” AlSi10Mg manufactured by SLM with different build orientations. Int J Fatigue 2020;139.

[20] Persenot T, Burr A, Martin G, Buffiere J-Y, Dendievel R, Maire E. Effect of build orientation on the fatigue properties of as-built electron beam melted Ti-6Al-4V alloy. Int J Fatigue 2019;118:65–76.

[21] du Plessis A, Beretta S. Killer notches: The effect of as-built surface roughness on fatigue failure in AlSi10Mg produced by laser powder bed fusion. Addit Manuf 2020;35.

[22] Pegues J, Roach M, Scott Williamson R, Shamsaei N. Surface roughness effects on the fatigue strength of additively manufactured Ti-6Al-4V. Int J Fatigue 2018;116(April):543–52.

[23] Schneller W, Leitner M, Pomberger S, Springer S, Beter F, Grün F. Effect of post treatment on the microstructure, surface roughness and residual stress regarding the fatigue strength of selectively laser melted AlSi10Mg structures. J Manuf Mater Process 2019;3(4):89.

[24] Dinh TD, Vanwalleghem J, Xiang H, Erdelyi H, Craeghs T, Van Paepegem W. A unified approach to model the effect of porosity and high surface roughness on the fatigue properties of additively manufactured Ti6-Al4-V alloys. Addit Manuf 2020;33:101139.

[25] Iliopoulos AP, Jones R, Michopoulos JG, Phan N, Rans C. Further studies into crack growth in additively manufactured materials. Materials 2020;13(10):2223.

[26] Mochache J, Taylor RM. A review of fatigue and damage tolerance life prediction methodologies toward certification of additively manufactured metallic principal structural elements. In: AIAA scitech 2021 forum. 2021, p. 1509.

[27] Tilson W, Wells D, McClung C. Developing approaches for certification of un-inspectable fracture critical AM Components. 2022, https://ntrs.nasa.gov/api/citations/20220015942/downloads/ICAM%202022%20-%20FC%20for%20Uninspectable%20AM%20Overview%20v2.pdf.

[28] Ghibaudo C, Maculotti G, Gobber F, Saboori A, Galetto M, Biamino S, et al. Information-rich quality controls prediction model based on non-destructive analysis for porosity determination of AISI H13 produced by electron beam melting. Int J Adv Manuf Technol 2023;126:1159–73. http://dx.doi.org/10.1007/s00170-023-11153-2.

[29] Bertolini R, Campagnolo A, Sorgato M, Ghiotti A, Bruschi S, Meneghetti G. Fatigue strength of LPBF Ti6Al4V machined under flood and cryogenic lubri-cooling conditions. Int J Fatigue 2022;162. http://dx.doi.org/10.1016/j.ijfatigue.2022.106973, Cited by: 1.

[30] Ghiotti A, Bertolini R, Sorgato M, Campagnolo A, Savio E, Bruschi S. Ti6Al4V titanium alloy fatigue strength after AM- and machining-based process chains. CIRP Annals 2022;71(1):461–4. http://dx.doi.org/10.1016/j.cirp.2022.04.021, Cited by: 2.

[31] Leach R. Optical measurement of surface topography. Springer, Berlin; 2011, http://dx.doi.org/10.1007/978-3-642-12012-1.

[32] Leach R, Bourell D, Carmignato S, Donmez A, Senin N, Dewulf W. Geometrical metrology for metal additive manufacturing. CIRP Ann 2019;68(2):677–700. http://dx.doi.org/10.1016/j.cirp.2019.05.004, URL https://www.sciencedirect.com/science/article/pii/S0007850619301611.

[33] Du Plessis A, Sperling P, Beerlink A, Kruger O, Tshabalala L, Hoosain S, et al. Standard method for microCT-based additive manufacturing quality control 3: Surface roughness. MethodsX 2018;5:1111–6.

[34] Leach R, Carmignato S. Precision metal additive manufacturing. CRC Press; 2020, http://dx.doi.org/10.1201/9780429436543.

[35] Galati M, Minetola P, Rizza G. Surface roughness characterisation and analysis of the electron beam melting (EBM) process. Materials 2019;12(13). http://dx.doi.org/10.3390/ma12132211, URL https://www.mdpi.com/1996-1944/12/13/2211.

[36] Jamshidinia M, Kovacevic R. The influence of heat accumulation on the surface roughness in powder-bed additive manufacturing. Surf Topogr: Metrol Prop 2015;3(1):014003. http://dx.doi.org/10.1088/2051-672X/3/1/014003.

[37] Newton L, Senin N, Gomez C, Danzl R, Helmli F, Blunt L, et al. Areal topography measurement of metal additive surfaces using focus variation microscopy. Addit Manuf 2019;25:365–89. http://dx.doi.org/10.1016/j.addma.2018.11.013, URL https://www.sciencedirect.com/science/article/pii/S2214860418306171.

[38] Gomez C, Su R, Thompson A, DiSciacca J, Lawes S, Leach RK. Optimization of surface measurement for metal additive manufacturing using coherence scanning interferometry. Opt Eng 2017;56(11):111714. http://dx.doi.org/10.1117/1.OE.56.11.111714.

[39] Maculotti G, Piscopo G, Marchiandi G, Atzeni E, Salmi A, Iuliano L. Build orientation effect on Ti6Al4V thin-wall topography by electron beam powder bed fusion. Procedia CIRP 2022;108:222–7. http://dx.doi.org/10.1016/j.procir.2022.03.039, 6th CIRP Conference on Surface Integrity. URL https://www.sciencedirect.com/science/article/pii/S2212827122005194.

[40] Maculotti G, Ghibaudo C, Genta G, Ugues D, Galetto M. An artificial intelligence classifier for electron beam powder bed fusion as-built surface topographies. CIRP J Manuf Sci Technol 2023;43:129–42.

[41] Galantucci L, Lavecchia F, Percoco G. Experimental study aiming to enhance the surface finish of fused deposition modeled parts. CIRP Ann 2009;58(1):189–92. http://dx.doi.org/10.1016/j.cirp.2009.03.071, URL https://www.sciencedirect.com/science/article/pii/S0007850609000778.

[42] Köpplmayr T, Häusler L, Bergmair I, Mühlberger M. Nanoimprint lithography on curved surfaces prepared by fused deposition modelling. Surf Topogr: Metrol Prop 2015;3(2):024003. http://dx.doi.org/10.1088/2051-672X/3/2/024003.

[43] Johnson MK, Cole F, Raj A, Adelson EH. Microgeometry capture using an elastomeric sensor. ACM Trans Graph 2011;30(4):1–8.

[44] Senin N, Thompson A, Leach RK. Characterisation of the topography of metal additive surface features with different measurement technologies. Meas Sci Technol 2017;28(9):095003. http://dx.doi.org/10.1088/1361-6501/aa7ce2.

[45] Kerckhofs G, Pyka G, Moesen M, Van Bael S, Schrooten J, Wevers M. High-resolution microfocus X-Ray computed tomography for 3D surface roughness measurements of additive manufactured porous materials. Adv Energy Mater 2013;15(3):153–8. http://dx.doi.org/10.1002/adem.201200156, URL https://onlinelibrary.wiley.com/doi/abs/10.1002/adem.201200156.

[46] Fox J, Kim F, Reese Z, Evans C. Complementary use of optical metrology and X-Ray computed tomography for surface finish and defect detection in laser powder bed fusion additive manufacturing, no. 69. In: Proceedings of the 2018 ASPE and euspen Summer Topical Meeting - Advancing Precision in Additive Manufacturing, Berkeley, CA. 2018, URL https://tsapps.nist.gov/publication/get_pdf.cfm?pub_id=926223.

[47] Townsend A, Pagani L, Scott P, Blunt L. Areal surface texture data extraction from X-ray computed tomography reconstructions of metal additively manufactured parts. Precis Eng 2017;48:254–64. http://dx.doi.org/10.1016/j.precisioneng.2016.12.008, URL https://www.sciencedirect.com/science/article/pii/S0141635916303518.

[48] Dewulf W, Bosse H, Carmignato S, Leach R. Advances in the metrological traceability and performance of X-ray computed tomography. CIRP Ann 2022;71(2):693–716. http://dx.doi.org/10.1016/j.cirp.2022.05.001, URL https://www.sciencedirect.com/science/article/pii/S0007850622001275.

[49] ASTM - American Society for Testing and Materials. ASTM F75-18.standard specification for cobalt-28 chromium-6 molybdenum alloy castings and casting alloy for surgical implants (UNS R30075), 2000. 2018.

[50] M2 series 5 cobalt chrome balanced+. 2023, https://www.ge.com/additive/sites/default/files/2020-07/M2SERIES5_COCRMO_CMDS_REV2.pdf. [Accessed 03 March 2023].

[51] Additive manufacturing takes flight – GE aviation’s integration of 3D printing to enable innovation. 2023, https://d3.harvard.edu/platform-rctom/wp-content/uploads/sites/4/2018/11/Comparison-left-305-parts-right-1-part.jpg. [Accessed 03 March 2023].

[52] Barricelli L, Patriarca L, du Plessis A, Beretta S. Orientation-dependent fatigue assessment of Ti6Al4V manufactured by L-PBF: Size of surface features and shielding effect. Int J Fatigue 2023;168:107401.

[53] ISO - International Organisation for Standardisation. ISO 25178-2:2012. Geometrical product specifications (GPS) - Surface texture: Areal - Part 2: Terms, definitions and surface texture parameters. 2012.
[54] ISO - International Organisation for Standardisation. ISO 25178-3:2012. Geometrical product specifications (GPS) - Surface texture: Areal - Part 3: Specification operators. 2012.
[55] Maculotti G, Genta G, Quagliotti D, Galetto M, Hansen HN. Gaussian process regression-based detection and correction of disturbances in surface topography measurements. Qual Reliab Eng Int 2022;38(3):1501–18. http://dx.doi.org/10.1002/qre.2980, URL https://onlinelibrary.wiley.com/doi/abs/10.1002/qre.2980.
[56] ISO - International Organisation for Standardisation. ISO 4288:1998. Geometrical product specifications (GPS) - Surface texture - Profile method: Rules and procedures for the assessment of surface texture. 1998.
[57] Scott PJ. The case of surface texture parameter RSm. Meas Sci Technol 2006;17:559–64.
[58] Seewig J, Scott PJ, Eifler M, Huser D. Crossing-the-line segmentation as a basis for rsm and rc evaluation. Surf Topogr: Metrol Prop 2020;8:024010.
[59] Murakami Y. Effect of size and geometry of small defects on the fatigue limit. Metal Fatigue 2002;35–55.
[60] Gockel J, Sheridan L, Koerper B, Whip B. The influence of additive manufacturing processing parameters on surface roughness and fatigue life. Int J Fatigue 2019;124(October 2018):380–8.
[61] Zhang J, Fatemi A. Surface roughness effect on multiaxial fatigue behavior of additive manufactured metals and its modeling. Theor Appl Fract Mech 2019;103.
[62] Nicoletto G. A novel test method for the fatigue characterization of metal powder bed fused alloys. Procedia Struct Integr 2017;7:67–74.
[63] Nicoletto G. Fatigue behavior of L-PBF metals: Cost-effective characterization via specimen miniaturization. J Mater Eng Perform 2021;30(7):5227–34.
[64] Narra SP, Rollett AD, Ngo A, Scannapieco D, Shahabi M, Reddy T, et al. Process qualification of laser powder bed fusion based on processing-defect structure-fatigue properties in Ti-6Al-4V. J Mater Process Technol 2023;311(August 2022):117775. http://dx.doi.org/10.1016/j.jmatprotec.2022.117775.
[65] Balachandramurthi AR, Moverare J, Dixit N, Pederson R. Influence of defects and as-built surface roughness on fatigue properties of additively manufactured alloy 718. Mater Sci Eng A 2018;735:463–74.
[66] Quagliotti D. Modeling the systematic behavior at the micro and nano length scales. Surf Topogr: Metrol Prop 2022;10(1):015011. http://dx.doi.org/10.1088/2051-672X/ac4ba7.
[67] ASTM - American Society for Testing and Materials. ASTM E739-10. Standard practice for statistical analysis of linear or linearized stress-life. Stat Anal Fatigue Data 2009;10(Reapproved 2015):129–129–9.
[68] JSME - Japan Society of Mechanical Engineers. JSME S 002. Standard method of statistical fatigue testing.
[69] Brownlee KA, Hodges Jr JL, Rosenblatt M. The up-and-down method with small samples. J Amer Statist Assoc 1953;48(262):262–77.
[70] Romano S, Brandão A, Gumpinger J, Gschweitl M, Beretta S. Qualification of AM parts: Extreme value statistics applied to tomographic measurements. Mater Des 2017;131:32–48. http://dx.doi.org/10.1016/j.matdes.2017.05.091, URL https://www.sciencedirect.com/science/article/pii/S0264127517305737.
[71] Wycisk E, Solbach A, Siddique S, Herzog D, Walther F, Emmelmann C. Effects of defects in laser additive manufactured Ti-6Al-4V on fatigue properties. Physics Procedia 2014;56:371–8.
[72] A comparison of fatigue strength sensitivity to defects for materials manufactured by AM or traditional processes. Int J Fatigue 2017;94:178–91.
[73] Masuo H, Tanaka Y, Morokoshi S, Yagura H, Uchida T, Yamamoto Y, et al. Influence of defects, surface roughness and HIP on the fatigue strength of Ti-6Al-4V manufactured by additive manufacturing. Int J Fatigue 2018;117:163–79.
[74] Meneghetti G, Rigon D, Gennari C. An analysis of defects influence on axial fatigue strength of maraging steel specimens produced by additive manufacturing. Int J Fatigue 2019;118:54–64.
[75] El Haddad MH, Smith KN, Topper TH. Fatigue crack propagation of short cracks. J Eng Mater Technol, Trans ASME 1979;101(1):42–6.
[76] Sausto F, Romano S, Patriarca L, Miccoli S, Beretta S. Benchmark of a probabilistic fatigue software based on machined and as-built components manufactured in AlSi10Mg by L-PBF. Int J Fatigue 2022;165:107171. http://dx.doi.org/10.1016/j.ijfatigue.2022.107171, URL https://www.sciencedirect.com/science/article/pii/S014211232200425X.